

- Nature* **384**, 623 (1996).
11. M. Coe and G. Bonan, *J. Geophys. Res.* **102**, 11087 (1997).
 12. S. L. Thompson and D. Pollard, *J. Clim.* **10**, 871 (1997).
 13. R. C. Pacanowski, K. W. Dixon, A. Rosati, "The GFDL Modular Ocean Model Users Guide, Version 1" (GFDL Ocean Group Tech. Rep. 2, Geophysical Fluid Dynamics Laboratory, Princeton, NJ, 1991).
 14. M. J. Rodwell and B. J. Hoskins, *Q. J. R. Meteorol. Soc.* **122**, 1385 (1996).
 15. B. J. Hoskins and D. J. Karoly, *J. Atmos. Sci.* **38**, 1179 (1981).
 16. S. Hastenrath, *Mon. Weather Rev.* **112**, 1097 (1984).
 17. K. Wolter, *J. Clim.* **2**, 149 (1989).
 18. P. J. Lamb, *Tellus A* **35**, 198 (1983).
 19. P. Chang, L. Ji, H. Li, *Nature* **385**, 516 (1997).
 20. This degree of monsoon enhancement was not found in earlier simulations of the climate of 6 or 9 ka that coupled an AGCM with a static mixed-layer ocean (27, 28). Our analysis of these earlier experiments and other simulations confirms that the SSTs and low-level atmospheric winds of the control simulation are substantially biased by the lack of ocean dynamics and that this bias in the control alters the atmospheric response to orbital forcing. Cooler equatorial waters and a more humid continental surface may also strengthen the monsoon by increasing the south-to-north gradient of equivalent potential temperature in the boundary layer over western North Africa [E. A. B. Eltahir and C. Gong, *J. Clim.* **9**, 1030 (1996)]; however, the change of this gradient is small in our simulation. Warmer North Atlantic waters poleward of the tropics may also cause precipitation to increase in North Africa, based on the results of a climate model experiment [P. B. deMenocal and D. Rind, *J. Geophys. Res.* **98**, 7265 (1993)]; this linkage may occur in our stimulation as well.
 21. P. Hoelzmann *et al.*, *Global Biogeochem. Cycles*, in press.
 22. A. McIntyre, W. F. Ruddiman, K. Karlin, A. C. Mix, *Paleoceanography* **4**, 19 (1989); A. McIntyre and B. Molino, *Science* **274**, 1867 (1996).
 23. W. F. Ruddiman and A. C. Mix, in *Global Climates Since the Last Glacial Maximum*, H. E. Wright Jr. *et al.*, Eds. (Univ. of Minnesota Press, Minneapolis, 1993), pp. 94–124.
 24. A. C. Mix, W. F. Ruddiman, A. McIntyre, *Paleoceanography* **1**, 43 (1986).
 25. In the equatorial Atlantic, three core sites indicate warmer than present conditions, and 10 core sites indicate colder than present conditions with a range of anomalies between 2°C and –2°C for August (23). The sites indicating colder than present conditions do not agree in sign with the long time series site (22), which indicated warmer conditions coinciding with perihelion in northern summer. In the northern subtropics, a site near the Bahamas at 25°N shows a mid-Holocene maximum in annual temperature (an increase of ~0.5°C) (24). Adjacent to the African coast, 20° to 25°N, two core sites indicate warmer than present conditions, and three core sites indicate colder than present conditions with a range of anomalies between 1.5° and –2.9°C for August (23). As in the equatorial Atlantic, the intercore differences are relatively large.
 26. Areas of particular future interest include the Arctic, where sea-ice cover almost certainly decreased (3, 27, 28); the Pacific, where there is evidence of changed El Niño–Southern Oscillation behavior [D. H. Sandweiss, J. B. Richardson III, E. J. Reitz, H. B. Rollins, K. A. Maasch, *Science* **273**, 1531 (1996)]; and the Indian Ocean, where changed upwelling in the Arabian Sea provided the first evidence for orbitally forced changes in monsoons [W. L. Prell, in *Milankovitch and Climate*, A. Berger *et al.*, Eds. (Reidel, Hingham, MA, 1984), pp. 349–366]. Changes in SSTs in these other ocean basins may also influence the climate of the Atlantic–African sector [(17); C. K. Folland, T. N. Palmer, D. E. Parker, *Nature* **320**, 602 (1986); T. N. Palmer, *ibid.* **322**, 251 (1986); S. Curtis and S. Hastenrath, *J. Geophys. Res.* **100**, 15835 (1995)]. On the basis of analogies with recent interannual variability [S. Hastenrath, *Climate and Circulation of the Tropics* (Reidel,

Dordrecht, Netherlands, 1985)], the SST changes in the tropical Atlantic that were simulated at 6 ka could also lead to changes in the mid-Holocene climate of eastern tropical South America.

27. J. E. Kutzbach and R. G. Gallimore, *J. Geophys. Res.* **93**, 803 (1988).
28. J. E. Kutzbach *et al.*, *Quat. Sci. Rev.*, in press.
29. We thank W. Xu, R. Gallimore, and P. Behling for assistance with model simulations and graphics; M. Kennedy for preparing the manuscript; and S. L.

Thompson and D. Pollard for allowing us to use the National Center for Atmospheric Research (NCAR) Genesis climate model. Supported by grants to the University of Wisconsin–Madison by the NSF's Climate Dynamics program and Earth System History program and by the U.S. Department of Energy. NCAR, which is sponsored by the NSF, provided computer resources.

23 July 1997; accepted 16 September 1997

Direct Observation of Cooling of Heme Upon Photodissociation of Carbonmonoxy Myoglobin

Yasuhisa Mizutani and Teizo Kitagawa*

The formation of vibrationally excited heme upon photodissociation of carbonmonoxy myoglobin and its subsequent vibrational energy relaxation was monitored by picosecond anti-Stokes resonance Raman spectroscopy. The anti-Stokes intensity of the ν_4 band showed immediate generation of vibrationally excited hemes and biphasic decay of the excited populations. The best fit to double exponentials gave time constants of 1.9 ± 0.6 and 16 ± 9 picoseconds for vibrational population decay and 3.0 ± 1.0 and 25 ± 14 picoseconds for temperature relaxation of the photolyzed heme when a Boltzmann distribution was assumed. The decay of the ν_4 anti-Stokes intensity was accompanied by narrowing and frequency upshift of the Stokes counterpart. This direct monitoring of the cooling dynamics of the heme cofactor within the globin matrix allows the characterization of the vibrational energy flow through the protein moiety and to the water bath.

Internal conversion processes after optical excitation or photoreactions leave the excited molecules or reaction products with excess energy. For small molecules the energy distributions in a molecule can be determined by transient absorption measurements (1), and these have provided considerable insight into intramolecular vibrational redistribution and vibrational cooling. For large molecules in condensed phases, however, the optical spectra are usually broad and featureless as a result of overlapping Franck-Condon transitions. For such systems, more direct monitoring of vibrational populations can be obtained, in principle, from time-resolved Raman (2, 3) and infrared spectroscopy (4). Time-resolved resonance Raman (TR³) spectroscopy is particularly suited for probing the vibrational state dynamics of colored molecules in solution phases. The ratio of the integrated areas of anti-Stokes and Stokes scattering, corrected to first order for reabsorption and cross section differences (3, 5), is expected to yield the most direct information about relative vibrational populations. Here, we applied this technique to explore the heating and cooling dynamics of heme in the globin matrix upon photol-

ysis of carbonmonoxy myoglobin (MbCO).

Myoglobin (Mb) is an oxygen-storage protein containing a heme prosthetic group (Fe^{II}-protoporphyrin IX). The heme is embedded within the globin and is linked to it through the proximal histidine. Small ligands such as O₂, CO, and NO bind reversibly to the sixth coordination site of Fe^{II}. These ligands are photodissociated on a femtosecond time scale by visible light (6–8). Although it was pointed out from sub-picosecond time-resolved infrared (TRIR) absorption of D₂O (9) that some excess energy remains in the photodissociated heme shortly after the photolysis, there has been no direct observation of vibrationally excited populations of the photodissociated heme in the picosecond time regime. Therefore, we constructed a system for picosecond TR³ measurements (10) and applied it to MbCO (11).

Stokes TR³ difference spectra of photodissociated Mb with 2.3-ps resolution were obtained for various delay times of the probe pulse from the pump pulse (Fig. 1). The fraction of photolyzed MbCO was estimated from the intensity loss of the Raman bands of MbCO to be about 30%. The TR³ spectrum in the 600 to 1500 cm⁻¹ region for 0-ps delay (Fig. 1) shows bands arising from the in-plane vibrations of heme at 1351, 1115, 781, and 672 cm⁻¹, which are assigned to ν_4 , ν_5 , ν_{32} , and ν_7 , respectively (12). These bands exhibited appreciable narrowing and frequency up-

Institute for Molecular Science, Okazaki National Research Institutes, Myodaiji, Okazaki 444, Japan.

*To whom correspondence should be addressed. E-mail: teizo@ims.ac.jp

shift in the first few picoseconds, but no further changes occurred after that. The TR³ spectrum for a 10-ps delay closely resembles the spectrum of deoxyMb, indicating that the photodissociated heme has relaxed to the equilibrium structure within a few picoseconds. This is consistent with the observations by Franzen *et al.* (6).

Detailed spectral changes of the ν_7 and ν_4 bands after photodissociation are shown in Fig. 2. At a delay of 1 ps, the center of the ν_4 band is located at 1351 cm⁻¹ and the band is broadened with a full width at half maximum (fwhm) of 37.9 ± 0.6 cm⁻¹. The band shifts to 1355 cm⁻¹ and becomes narrower (fwhm = 28.4 ± 0.6 cm⁻¹) at 50-ps delay. Time constants of the band shift and narrowing were 2.1 ± 0.7 and 1.4 ± 0.8 ps, respectively. Similar trends are observed for the ν_7 band, which is centered at 672 cm⁻¹ and is broadened (fwhm = 29.7 ± 0.7 cm⁻¹) for 1-ps delay, but is shifted to 676 cm⁻¹ and becomes narrower (fwhm = 26.4 ± 0.7 cm⁻¹) for 50-ps delay. Similar features have also been observed for nickel octaethylporphyrin in toluene (13).

Anti-Stokes Raman intensity is expected to be the most direct probe of the extent and dissipation rate of excess vibrational energy. No bands of MbCO were recogniz-

able in the raw anti-Stokes spectra in contrast to the raw Stokes spectra. This means that the high-frequency vibrations of the heme are not excited unless CO is photolyzed. In the anti-Stokes TR³ difference spectra between -5 and 50 ps (Fig. 3), intensities are highest at 1-ps delay, when the ν_3 , ν_4 , ν_5 , and ν_{32} bands are observed at 1461, 1350, 1112, and 779 cm⁻¹, respectively. These bands lose intensity as the delay time increases and have completely disappeared at 50-ps delay. It should be noted that no peak was observed in the ν_7 region. Although a weak ν_7 band is compatible with reported results (14), the ν_7 band could be expected to have comparable intensity to that of ν_4 on the basis of the Stokes spectra in Fig. 1 and under the assumption of a statistical distribution of vibrational energy, if Raman cross sections for ν (vibrational quantum number) = 0 ← 1 (anti-Stokes) and $\nu = 1 \leftarrow 0$ (Stokes) transitions are alike (15). Even if their differences are not negligible, the anti-Stokes ν_7 band is too weak, suggesting the occurrence of a mode-specific relaxation of vibrational energy.

Investigation of the temporal behavior of the Raman intensities (Fig. 4) shows that the Stokes intensity (Fig. 4A) develops within the instrument response and remains constant. This is consistent with the fact that the photodissociation of CO from the heme takes place within a few hundred femtoseconds (7) and that recombination of CO to the heme takes place in the time regime of hundreds of microseconds (16). The temporal behavior of Stokes intensity is comparable with the transient absorption spectrum (Fig. 4B). The anti-Stokes intensity (Fig. 4C) develops within the instrument response time. The instrument response was

deconvoluted from the decay of the anti-Stokes intensity by using a Gaussian fit (2.3-ps fwhm) to the cross correlation signal. The solid and broken lines in Fig. 4C denote the best fit double- and single-exponential decays, respectively. The former can reasonably reproduce the observed points, whereas the latter fails to reproduce the observations in the range from 10 to 30 ps (17). This analysis gave the decay constants of 1.9 ± 0.6 ps (93%) and 16 ± 9 ps (7%), the former of which is compatible with the time constants of the Stokes band shift (2.1 ± 0.7 ps) and narrowing (1.4 ± 0.8 ps). Because there is no intensity change in the Stokes ν_4 band in the 3- to 50-ps time range, the observed intensity decay in the anti-Stokes ν_4 band can be ascribed to vibrational energy relaxation.

A 540-nm photon excites the heme into the $\pi\pi^*$ state [¹Q(1, 0)], thereby depositing 221 kJ/mol of energy. The $\pi\pi^*$ -excited heme is believed to relax to a level having an antibonding character of the Fe-CO bond, although the energy of the Fe-CO antibonding level has not yet been determined. The absorbed photon energy is significantly higher than the energy required to break the Fe-CO bond, and therefore excess energy is left on the photolyzed heme. The enthalpy difference between Mb + CO (gas) and MbCO is ~90 kJ/mol (18), so that the heme and CO share ~130 kJ/mol of excess energy. Partitioning of this excess energy depends on a relaxation mechanism. If the ⁵T₂ or ³T₁ state of Fe^{II} were involved, as was suggested for hemoglobin-CO (HbCO) (19), the heme would have an excess energy of 50 to 100 kJ/mol right after the photodissociation.

Pioneering work on the energy flow from the heme into the protein matrix was reported by Henry *et al.* (20), who carried out molecular dynamics simulations for Mb and

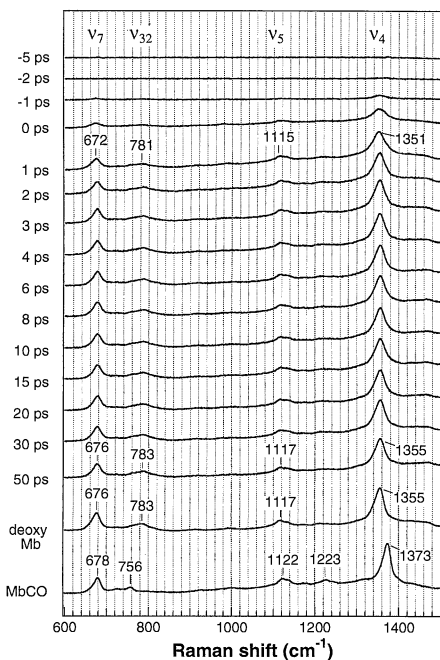


Fig. 1. TR³ spectra on the Stokes side of photo-dissociated MbCO for time delays from -5 to 50 ps. The TR³ difference spectra were obtained by subtracting the probe-only spectrum from the pump-probe spectra with an appropriate factor. Spectral intensities were corrected for absorbance changes by using the intensity of the 980 cm⁻¹ band of sulfate ions present in the solution. Stokes spectra of the equilibrium deoxyMb and MbCO are depicted for comparison.

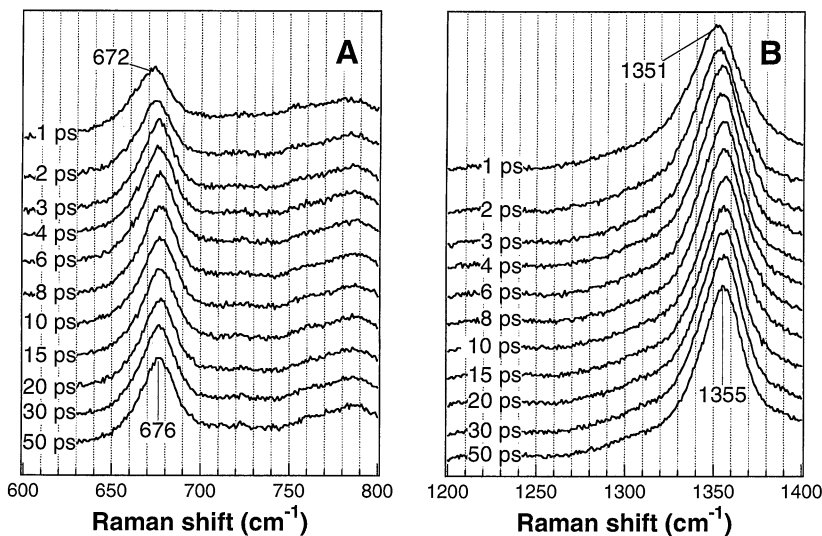


Fig. 2. Close-ups of time-resolved Stokes Raman spectra in the ν_7 (A) and ν_4 (B) region.

cytochrome c with initial energy deposits corresponding to optical excitation at both 532 and 355 nm. The simulation predicted a fast initial relaxation phase with decay constants of 1 to 4 ps followed by a slower relaxation phase with decay constants of 20 to 40 ps. To compare our results with these predictions, it is necessary to estimate the temperature decay rate of the heme. The anti-Stokes/Stokes Raman intensity ratio is determined by the Boltzmann factor for the vibrational mode in question under the assumption of a statistical distribution of the vibrational energy. When the observed kinetics of population decay in vibrationally excited states are converted to temperatures by assuming a Boltzmann distribution, the time constants of 1.9 ± 0.6 and 16 ± 0.9 ps for the population decay give rise to time constants of 3.0 ± 1.0 and 25 ± 14 ps, respectively, for the temperature decay. These values appear to be close to the value predicted by Henry *et al.* (20). However, the molecular dynamics simulations suggest a ratio of 50:50 for the magnitudes of the fast and the slow components, whereas the amplitude ratio in Fig. 4C is 93:7. It is noted that the simulation was conducted in vacuo and neglected the effect of the water bath, which would serve as an extensive thermal sink. In fact, fast heating of water with a time constant of 7.5 ± 1.5 ps was observed for Mb in D₂O (21). Neglecting the effects of the water bath may decelerate the cooling rate of heme, resulting in a larger contribution of the slow component. Anfirud

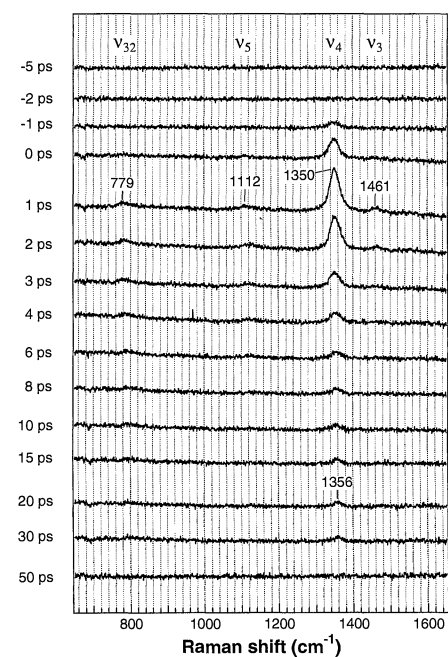


Fig. 3. TR³ spectra on the anti-Stokes side of photodissociated MbCO for time delays from -5 to 50 ps. The spectra are represented as difference spectra relative to the probe-only spectrum.

and co-workers (22) analyzed the temporal behavior of band III of photoexcited deoxyMb (763 nm) with femtosecond near-infrared absorption and obtained 6.2 ± 0.5 ps for a cooling time constant of the heme in the ground electronic state. The cooling rate from the band III behavior corresponds to an average of relaxation rates of various vibrational modes and is presumably longer than the cooling rate of the high-frequency ν_4 mode (3.0 ps).

Hopkins and co-workers have measured TR³ spectra of deoxyHb with a time resolution of 8 ps (23). Intensity changes of both negative transients in Stokes and positive transients in anti-Stokes showed population changes with time constants of 2 to 5 ps, to which the 1.9-ps decay of Fig. 4C obtained with higher time resolution is comparable, despite the differences in the globin (Mb versus Hb) and in phenomena (CO-photodissociation versus electronic

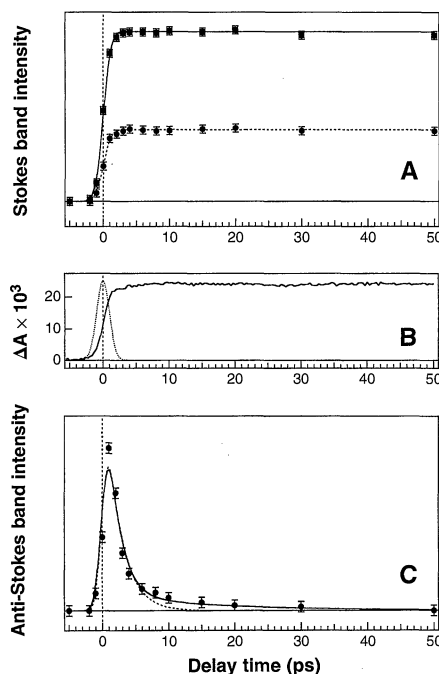


Fig. 4. (A) Temporal profiles of intensities of the Stokes ν_4 (circles) and ν_7 (squares) bands. The solid and broken lines are the best fit to a step function (assuming instantaneous rise and very slow decay) for the ν_4 and ν_7 bands, respectively. (B) Temporal profile of absorbance ΔA of deoxyMb at 435 nm after excitation at 540 nm. The cross correlation traces between the pump and probe pulses are depicted by a dotted line. (C) Temporal profiles of anti-Stokes intensity of the ν_4 band (circles). The solid lines are the best fit to a double-exponential decay convoluted with the instrument response function, and the obtained decay time constants were 1.9 ± 0.6 (93%) and 16 ± 9 ps (7%). The broken line is the best fit to a single-exponential decay convoluted with the instrument response function, and the obtained decay constant was 2.3 ± 0.8 ps.

excitation). Petrich *et al.* studied vibrational relaxation of heme-containing proteins indirectly using femtosecond Stokes resonance Raman spectroscopy and estimated the temperature of heme in HbCO from the band shift of the ν_4 (8). They concluded that the heme in the HbCO photoproduct was substantially cooled within 10 ps, in agreement with our results on the time scale of vibrational cooling.

The fast energy dissipation from the globin to the water bath has also been noted by femtosecond TRIR studies, which monitor the heating of water that results from photoexcitation of deoxyMb (21). The observed kinetics was fitted with a model having two time constants. The fast component was best fitted by a Gaussian rise function with a time constant of 7.5 ± 1.5 ps, and the slow component was described by a time constant of ~ 20 ps with 40% of the total amplitude. We emphasize that the ratios of the contributions of the two components differ between the water heating (TRIR) and heme cooling (TR³) studies, although both exhibit biphasic responses. Therefore, the two components observed in the heme cooling may not directly correspond to the heating of the water bath; rather, it suggests that most (93%) of the heme excess energy dissipates into the globin in the fast component, but that there are two channels of energy dissipation from the protein to the water bath. One is through a classical diffusion process and is responsible for the slow component; the observed time constant is in reasonable agreement with that calculated from classical diffusion theory. The other channel is through the collective motions of the protein (21) and is responsible for the fast component. The time constant of heme cooling (3.0 ps) is shorter than that of water heating (7.5 ps). This time lag may correspond to the time taken for energy propagation through collective low-frequency modes of the protein. It should be possible in the near future to obtain mode-specific dynamical information, thereby allowing determination of the rates of intramolecular vibrational redistribution and vibrational cooling processes in solution or protein matrices.

REFERENCES AND NOTES

1. T. Elsaesser and W. Kaiser, *Annu. Rev. Phys. Chem.* **42**, 83 (1991); R. J. Senson, S. T. Repinec, A. Z. Szarka, R. M. Hochstrasser, *J. Chem. Phys.* **98**, 6291 (1993).
2. D. L. Phillips, J.-M. Rodier, A. B. Myers, *Chem. Phys.* **175**, 1 (1993); P. Matousek *et al.*, *Chem. Phys. Lett.* **237**, 373 (1995); S. Schultz, J. Qian, J. M. Jean, *J. Phys. Chem. A* **101**, 1000 (1997).
3. T. Nakabayashi, H. Okamoto, M. Tasumi, *J. Phys. Chem. A* **101**, 3494 (1997).
4. H. J. Bakker, P. C. M. Planken, A. Lagendijk, *Nature* **347**, 745 (1990); M. Li *et al.*, *J. Chem. Phys.* **98**, 5499 (1993); D. Raftery, E. Gooding, A. Romanovsky, R. M. Hochstrasser, *ibid.* **101**, 8572 (1994).

5. K. T. Schomacker, O. Bangcharoenpaupong, P. M. Champion, *J. Chem. Phys.* **80**, 4701 (1997).
6. S. Franzen, B. Bohn, C. Poyart, J. L. Martin, *Biochemistry* **34**, 1224 (1995).
7. J. L. Martin *et al.*, *Proc. Natl. Acad. Sci. U.S.A.* **80**, 173 (1983).
8. J. W. Petrich, J. L. Martin, D. Houde, C. Poyart, A. Orszag, *Biochemistry* **26**, 7914 (1987).
9. P. A. Anfirud, C. Han, R. M. Hochstrasser, *Proc. Natl. Acad. Sci. U.S.A.* **86**, 8387 (1989).
10. Seed pulses from a mode-locked Ti:sapphire oscillator (Tsunami 3950, Spectra-Physics) were put into a regenerative amplifier (Spitfire, Positive Light) pumped by an Nd:yttrium-lithium-fluoride (Nd:YLF) laser operated at 1 kHz. The amplified output was composed of 2.5-ps pulses with energies of ~0.6 mJ at 784 nm. The pump pulse at 540 nm was generated with a homemade optical parametric generator (OPG) and amplifier (OPA), which were pumped with the second harmonic of the 784-nm output. (For details about the OPG-OPA system, see Y. Uesugi, Y. Mizutani, T. Kitagawa, *Rev. Sci. Instrum.*, in press.) The probe pulse at 435 nm was generated as the first Stokes stimulated Raman scattering from compressed (50 kg/cm²) methane gas excited by the second harmonic of the 784-nm output. The energy and bandwidth of the OPG-OPA output were 30 μ J and ~3 nm, respectively, and the pulses were used for the pump beam in the present TR³ measurements after they were attenuated to 10 μ J with a Cr-coated quartz neutral density filter. The energy and bandwidth of the stimulated Raman scattering were 1.0 to 1.5 μ J and 14 cm⁻¹, respectively. The pump and probe beams were collinearly combined with a dichroic mirror. The polarization of the pump beam was rotated by 55° relative to that of the probe beam to minimize the effects of molecular rotations on the observed kinetics. Both beams were always monitored with photodiodes and found to be stable within \pm 10%. Raman scattering was collected and focused onto the entrance slit of a single-stage imaging spectrograph (500IM-CM, Chromex) by using two doublet achromats. A dichroic filter was placed between the lenses to reject the scattered pump beam. A holographic notch filter (Kaiser Optical Systems) was used to reject the unshifted scattering. A polarization scrambler was placed at the entrance slit to remove the effects of polarization from the spectrograph throughput. The spectrograph was equipped with a blazed-holographic grating (2400 grooves per millimeter), which enables us to measure a spectrum as wide as ~900 cm⁻¹ in the Soret region with a spectral slit width of 10 cm⁻¹. The dispersed light was detected with a liquid nitrogen-cooled charge-coupled device detector (CCD-1100PB, Princeton Instruments). The 0 ps of delay time (uncertainty < 0.2 ps) was calibrated at the probe wavelength by using rhodamine 6G in methanol. The cross correlation width between the pump and probe pulses measured with a 1-mm β -barium borate crystal was 2.3 ps. Raman shifts were calibrated with indene. Peak positions of Raman bands are accurate within \pm 2 cm⁻¹.
11. Horse skeletal Mb (Sigma, type M630) was dissolved into deoxygenated buffer (50 mM tris-HCl, pH 8.0). The concentrated Mb solution was reduced by sodium dithionite, bubbled with CO gas, and subjected to gel filtration through a Sephadex G-25 column. The solution was diluted to 100 μ M with deoxygenated and CO-saturated buffer (50 mM tris-HCl, pH 8.0) and put into an airtight quartz cuvette under a CO atmosphere. The sample solution in the cell was continuously stirred during the measurements to prevent multiple probing of the same portion of sample. Data accumulation time was 10 and 120 min for Stokes and anti-Stokes spectra, respectively. Sample integrity was confirmed with ultraviolet-visible absorption spectra after the TR³ measurements.
12. M. Abe, T. Kitagawa, Y. Kyogoku, *J. Chem. Phys.* **69**, 4526 (1978).
13. S. Sato and T. Kitagawa, *Appl. Phys. B* **59**, 415 (1994); S. G. Kruglik, Y. Mizutani, T. Kitagawa, *Chem. Phys. Lett.* **266**, 283 (1997).
14. M. C. Simpson *et al.*, *J. Am. Chem. Soc.* **119**, 5110 (1997).
15. The Boltzmann factor was represented in terms of the resonant Stokes and anti-Stokes scattering intensities in (5). With this expression we can, in principle, correct the differences between the Stokes and anti-Stokes scattering cross sections and determine an effective temperature of vibrational modes by analyzing their Raman excitation profiles.
16. Q. H. Gibson, J. S. Olson, R. E. McKinnie, R. J. Rohlfis, *J. Biol. Chem.* **261**, 10228 (1986).
17. P. Li and P. M. Champion [*Biophys. J.* **66**, 430 (1994)] used the two-boundary thermal transport model to analyze the thermal response to instantaneous heating of a chromophore embedded in a protein surrounded by water. The numerical solution of this model was well described by a double-exponential function in the short time limit, which "rolled over" into a diffusion-limited $t^{-3/2}$ decay (where t is time) in the long time limit.
18. M. H. Keyes, M. Falley, R. Lumry, *J. Am. Chem. Soc.* **93**, 2035 (1971).
19. B. I. Greene, R. M. Hochstrasser, R. B. Weisman, W. A. Eaton, *Proc. Natl. Acad. Sci. U.S.A.* **75**, 5255 (1978).
20. E. R. Henry, W. A. Eaton, R. M. Hochstrasser, *ibid.* **83**, 8982 (1986).
21. T. Lian, B. Locke, Y. Kholodenko, R. M. Hochstrasser, *J. Phys. Chem.* **98**, 11648 (1994).
22. M. Lim, T. A. Jackson, P. A. Anfirud, *ibid.* **100**, 12043 (1996).
23. J. R. Lingle, X. Xu, H. Zhu, S.-C. Yu, J. B. Hopkins, *ibid.* **95**, 9320 (1991).
24. Y.M. is a recipient of an Inoue Research Award for Young Scientists and gratefully acknowledges the Inoue Foundation for Science for partial support of this study. Supported by Grant-in-Aids for Scientific Research on Priority Areas (08249106) to T.K. from the Ministry of Education, Science, Sports, and Culture, Japan.

23 June 1997; accepted 2 September 1997

DNA Solution of the Maximal Clique Problem

Qi Ouyang,* Peter D. Kaplan, Shumao Liu, Albert Libchaber

The maximal clique problem has been solved by means of molecular biology techniques. A pool of DNA molecules corresponding to the total ensemble of six-vertex cliques was built, followed by a series of selection processes. The algorithm is highly parallel and has satisfactory fidelity. This work represents further evidence for the ability of DNA computing to solve NP-complete search problems.

Computer scientists rank computational problems in three classes: easy, hard, and uncomputable (1). Recently, Adleman (2) showed that DNA can be used to solve a computationally hard problem, the Hamiltonian path problem, and demonstrated the potential power of parallel, high-density computation by molecules in solution. This parallelism allows DNA computers to solve larger hard problems such as NP-complete problems in linearly increasing time, in contrast to the exponentially increasing time required by a Turing machine. The trade-off is that DNA computers require exponentially increasing volumes of DNA. The ultimate success of DNA computing will be found in the details of algorithms taking advantage of massive parallelism. Despite valuable theoretical work (3, 4), experiments of similar complexity to Adleman's have been few (5). Here, we present a molecular biology-based experimental solution to the maximal clique problem. We show (i) the solution to a problem in the same class (NP-complete) as the Hamiltonian path problem, (ii) a functional demonstration

of improved design principles for DNA computing, and (iii) the use of living organisms (*Escherichia coli*) to read the answer of a computation.

Mathematically, a clique is defined as a set of vertices in which every vertex is connected to every other vertex by an edge. The maximal clique problem asks: Given a network containing N vertices and M edges, how many vertices are in the largest clique? The graph of six vertices and 11 edges in Fig. 1a defines such a problem. The vertices (5,4,3,2) form the largest clique; thus, the size of the largest clique in this network is four. Finding the size of the largest clique has been proven to be an NP-complete problem (6). We designed the following algorithm to solve it:

1) For a graph with N vertices, each possible clique is represented by an N -digit binary number. A bit set to 1 represents a vertex in the clique, and a bit set to 0 represents a vertex out of the clique. For example, the clique (4,1,0) is represented by the binary number 010011, whereas (5,4,3,2), the largest clique in Fig. 1a, is represented by the number 111100. In this way, we transform the complete set of possible cliques in an N -vertex graph into an ensemble of all N -digit binary numbers. We call this the complete data pool.

2) We find pairs of vertices in the graph that are not connected by an edge. The graph containing all edges missing in the

Q. Ouyang and P. D. Kaplan, NEC Research Institute, 4 Independence Way, Princeton, NJ 08540, USA.

S. Liu and A. Libchaber, NEC Research Institute, 4 Independence Way, Princeton, NJ 08540, USA, and Center for Studies in Physics and Biology, Rockefeller University, New York, NY 10021, USA.

*To whom correspondence should be addressed.